

High-Speed Mid-Wave Infrared InAs/InAsSb Superlattice Uni-Traveling Carrier Photodetectors With Different Absorber Doping

Jian Huang^{ID}, Zhecheng Dai^{ID}, Zhijian Shen^{ID}, Zongti Wang, Zhiqi Zhou, Ziyu Wang, Bo Peng, Weimin Liu, and Baile Chen^{ID}, *Senior Member, IEEE*

Abstract—In this article, we studied two high-speed mid-wave infrared InAs/InAsSb type-II superlattice (T2SL) uni-traveling carrier (UTC) photodetectors (PDs) with different graded p-doping profiles in the absorber. It is found that the UTC device with higher absorber p-doping (hereafter referred to as Device A) has a larger 3-dB bandwidth than that of the device with lower absorber p-doping (hereafter referred to as Device B). However, Device A shows a higher dark current and lower responsivity performance than Device B. The peak responsivity of Devices A and B is about 0.9 and 1.2 A/W, respectively, under -1 V at room temperature. The performance comparisons of both devices are explored in detail. These results could contribute a further step toward developing high-speed InAs/InAsSb T2SL PDs.

Index Terms—High-speed photodetectors (PDs), InAs/InAsSb type-II superlattices (T2SL), mid-wavelength infrared (MWIR) photodetectors, uni-traveling carrier (UTC) photodetectors.

I. INTRODUCTION

FREE-SPACE optical communication (FSOC) in the mid-wavelength infrared (MWIR) transmission window has

Manuscript received 28 July 2022; revised 7 October 2022; accepted 26 October 2022. Date of publication 7 November 2022; date of current version 30 November 2022. This work was supported in part by the National Key Research and Development Program of China under Grant 2019YFB2203400, in part by the National Natural Science Foundation of China under Grant 61975121, and in part by the Double First-Class Initiative Fund of ShanghaiTech University. The review of this article was arranged by Editor J. D. Phillips. (Jian Huang and Zhecheng Dai contributed equally to this work.) (Corresponding author: Baile Chen.)

Jian Huang, Zhecheng Dai, Zhijian Shen, Zongti Wang, and Zhiqi Zhou are with the School of Information Science and Technology, ShanghaiTech University, Shanghai 201210, China (e-mail: huangjian@shanghaitech.edu.cn; daizhch@shanghaitech.edu.cn; shenzhj1@shanghaitech.edu.cn; wangzt@shanghaitech.edu.cn; zhouzq@shanghaitech.edu.cn).

Ziyu Wang, Bo Peng, and Weimin Liu are with the School of Physical Science and Technology, ShanghaiTech University, Shanghai 201210, China (e-mail: wangzy8@shanghaitech.edu.cn; pengbo@shanghaitech.edu.cn; liuwm@shanghaitech.edu.cn).

Baile Chen is with the School of Information Science and Technology, ShanghaiTech University, Shanghai 201210, China, and also with the Shanghai Engineering Research Center of Energy Efficient and Custom AI IC, Shanghai 201210, China (e-mail: chenbl@shanghaitech.edu.cn).

Color versions of one or more figures in this article are available at <https://doi.org/10.1109/TED.2022.3218489>.

Digital Object Identifier 10.1109/TED.2022.3218489

recently become an option of interest due to its stable performance through atmospheric channel perturbation such as dust, fog, and turbulence [1], [2], [3]. A high-speed MWIR photodetector (PD) to facilitate the benefits of the MWIR FSOC becomes important. Moreover, the recently developed dual-frequency comb spectroscopy, which can precisely define the molecular hyperfine structure, also requires high-speed mid-wave infrared PDs. [4], [5], [6], [7]. However, the current research on the MWIR PDs mainly focused on improving the signal-to-noise ratio performance; the speed performance of the device was rarely studied. There are a few architectures based on intersubband transition, such as quantum well infrared PD (QWIP) [8] and quantum cascade detectors (QCDs) [9], showing high 3-dB bandwidth performance in both MWIR and long-wavelength infrared band. However, these devices are narrow-band and often suffer from high dark current or low responsivity.

Antimonide-based type-II superlattices (T2SLs) based on the interband transition have emerged as a promising candidate for infrared PDs application with a broadband optical response. For the high-speed operation in the MWIR range, our group first reported MWIR uni-traveling carrier (UTC) PDs based on InAs/GaSb T2SL [10]. The UTC structure takes advantage of the fast electron transport and the neglectable dielectric relaxation time of the hole, thus could achieve an excellent device bandwidth performance, and has been widely used in the near-infrared band [11], [12], [13], [14], [15], [16], [17]. The device exhibits a decent 3-dB bandwidth of 6.58 GHz. However, the responsivity is still low due to the thin absorber used to achieve high-speed operation.

Compared to InAs/GaSb T2SL, Ga-free InAs/InAsSb T2SL enjoys the advantage of the long minority carrier time and tractable material growth, which has emerged recently as a versatile infrared material reported by many research groups [18], [19], [20], [21], [22], [23]. In order to improve the responsivity of high-speed MWIR UTC PDs, we initially designed a UTC PD based on InAs/InAsSb superlattice (SL) (referred to as Device A) [24]. The device shows a responsivity of 0.6 A/W at $4.5 \mu\text{m}$ under -1 V and a 3-dB bandwidth of 12.8 GHz under -4 V at room temperature. Although the bandwidth value of the device leads the reported Sb-based PDs

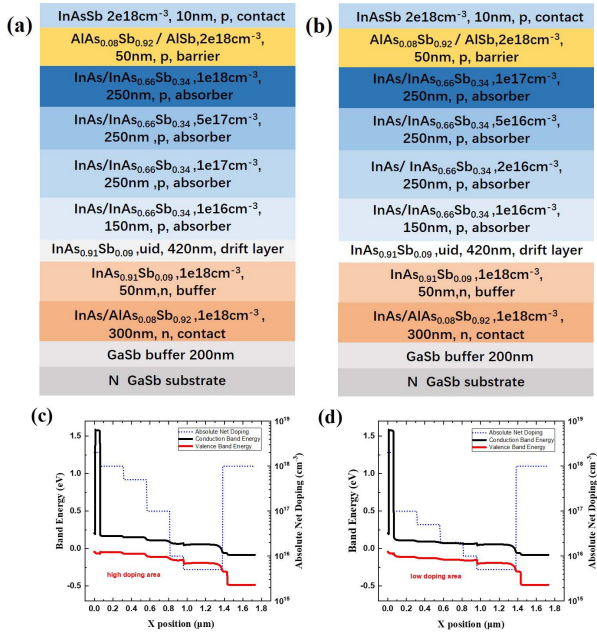


Fig. 1. Epitaxial structure of the designed device: (a) sample A and (b) sample B. Energy band diagram and absolute net doping of the designed device: (c) sample A and (d) sample B.

operating in the mid-wave infrared range, the detectivities of the devices are still lower than the state of the art. To further explore the devices' mechanism and optimize the performance, we design another InAs/InAsSb UTC device structure with a lower absorber doping profile for comparison (referred to as Device B). The performance of both devices has been investigated and compared comprehensively in this work. The experimental results show that the cutoff wavelength of both devices is about $5.5 \mu\text{m}$ at room temperature. Benefiting from a smaller electric field distribution in the depleted region and lower carrier recombination rates, Device B, with a lower doped absorber, has a low dark current and higher responsivity performance. The peak responsivity is about 0.9 and 1.2 A/W under -1 V at room temperature for Devices A and B, respectively. However, the longer hole transit time in the lower doped absorber results in a lower 3-dB bandwidth for Device B compared to that of Device A. As the applied reverse voltage increases, a bandwidth-enhancement phenomenon emerges for both devices. This bandwidth-enhancement phenomenon has also been investigated and discussed in detail in this work. Furthermore, the limitations on the 3-dB bandwidth of these devices have been explored by analyzing the equivalent circuit model and carrier transit-time-limited frequency response simulation. These results could provide insights for developing high-speed InAs/InAsSb PDs further.

II. DEVICE STRUCTURE AND FABRICATION

These two samples were grown on an n-type GaSb substrate by the molecular beam epitaxy system (MBE). As shown in Fig. 1(a) and (b), the epitaxial growth started with a GaSb buffer on an n-type GaSb substrate, followed by an InAs/AlAsSb SL bottom contact. After that, an unintentionally doped InAsSb drift layer was grown, followed by an

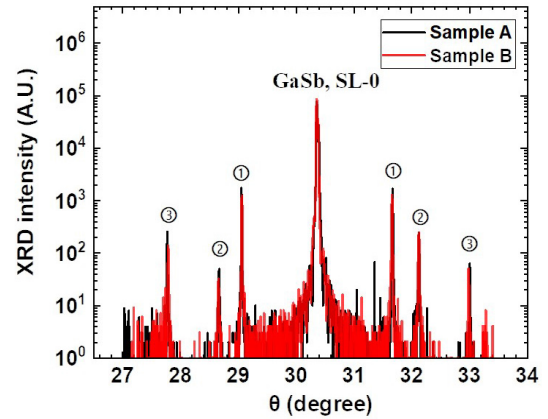


Fig. 2. HRXRD scan of the growth samples. Black line: sample A and Red line: sample B.

InAs/InAsSb SL absorption layer with different four-step graded doping. Then, an AlAsSb/AlSb SL layer was grown as the electron barrier, followed by an InAsSb layer as the top contact. Here, the absorption layer of sample A was grown with a higher graded p-doping level from 1×10^{18} to $1 \times 10^{16} \text{ cm}^{-3}$ [24], while the p-doping of sample B was graded from 1×10^{17} to $1 \times 10^{16} \text{ cm}^{-3}$, as shown in Fig. 1. Energy band diagrams, together with the doping concentration of two samples, have also been plotted to distinguish the different designs of graded doping, as shown in Fig. 1(c) and (d). High-resolution X-ray diffraction (HRXRD) measurement was used to investigate the crystal quality, as shown in Fig. 2. As can be seen, the satellite peaks of these two samples coincide well, suggesting that the compositions of these two samples are close. The SL satellite peaks are sharp, and the 0th satellite peak of the SL matched to the GaSb substrate. As shown in Fig. 2, peaks 1 and 3 are the ± 1 th and ± 2 th satellite peaks of InAs/InAsSb absorption SL, while peak 2 is the ± 1 th satellite peaks of InAs/InAsSb. According to the HRXRD curve, the thickness of single period InAs/InAsSb SL and InAs/AlAsSb SL is calculated [25] to be around 3.91 and 2.95 nm, respectively, which match the designed values. After material growth, these two samples were processed into circle mesa-shaped devices for device characterizations. Details of device fabrication can also be found in [24].

III. RESULTS AND DISCUSSION

After device fabrication, we first investigated the electrical characterization of these two devices. Fig. 3(a) shows the measured dark current ($I-V$) curve of these two devices with a diameter of $20 \mu\text{m}$ at different temperatures. Fig. 3(b) shows the dark current density at -0.1 V as a function of ratio of perimeter to area (P/A), along with the linear fit for both devices. The intercepts represent the bulk dark current density, while the slopes indicate the surface leakage current density [26]. The dark current of Device A at room temperature is higher than that of Device B. Since the surface leakage components of the two devices shown in Fig. 3(b) are very close, the primary source of the dark current difference between the two devices comes from the bulk

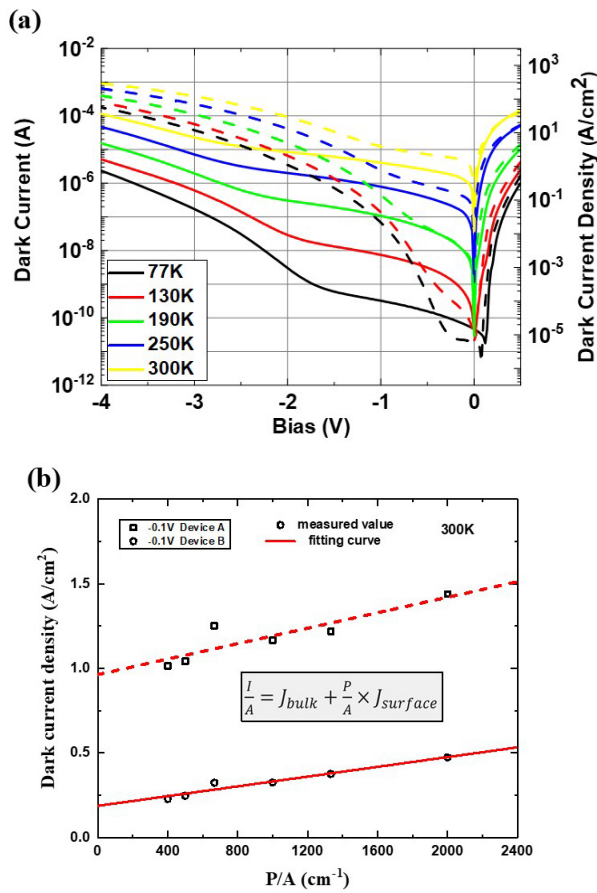


Fig. 3. (a) I - V characterization of devices as a function of temperature. (b) Dark current density as a function of P/A and linear fit under -0.1 -V bias at room temperature for both devices. For the function, I is the dark current, A is the device area, J_{bulk} is the bulk current density, P is the device perimeter, and J_{surface} is the surface leakage current density. Dashed line: Device A and solid line: Device B.

component difference due to the Auger recombination. Compared with Device B, tunneling current occurs more obviously at lower temperatures and higher reverse bias in Device A. As the temperature rises from 77 to 300 K, the dark current density of Device A increases from 0.02 to 3.94 A/cm² at -1 V, while Device B changes from 6.32×10^{-5} to 0.89 A/cm² at -1 V. At lower bias (below -0.5 V), the I - V curves of these two devices behave similarly, while at high bias, Device A shows a larger tunneling current than Device B. This is because Device A has a narrower depletion region and, thus, a higher electrical field in the depleted absorber than that of Device B, given the higher absorber doping in Device A.

After electrical characterization, the optical performances of the devices were studied. Fig. 4(a) shows the responsivity of these devices at different temperatures under zero bias. As the temperature goes from 77 to 300 K, the cutoff wavelength of both devices shifts from 4.5 to 5.5 μm . The peak responsivity at 77 K for Devices A and B is about 0.88 and 1.25 A/W and decreases to 0.25 and 0.6 A/W at 300 K, respectively. The responsivity reaches a peak at about 200 K because of the tradeoff between the absorption coefficient and the minority carrier lifetime [27]. The lower responsivity of Device A

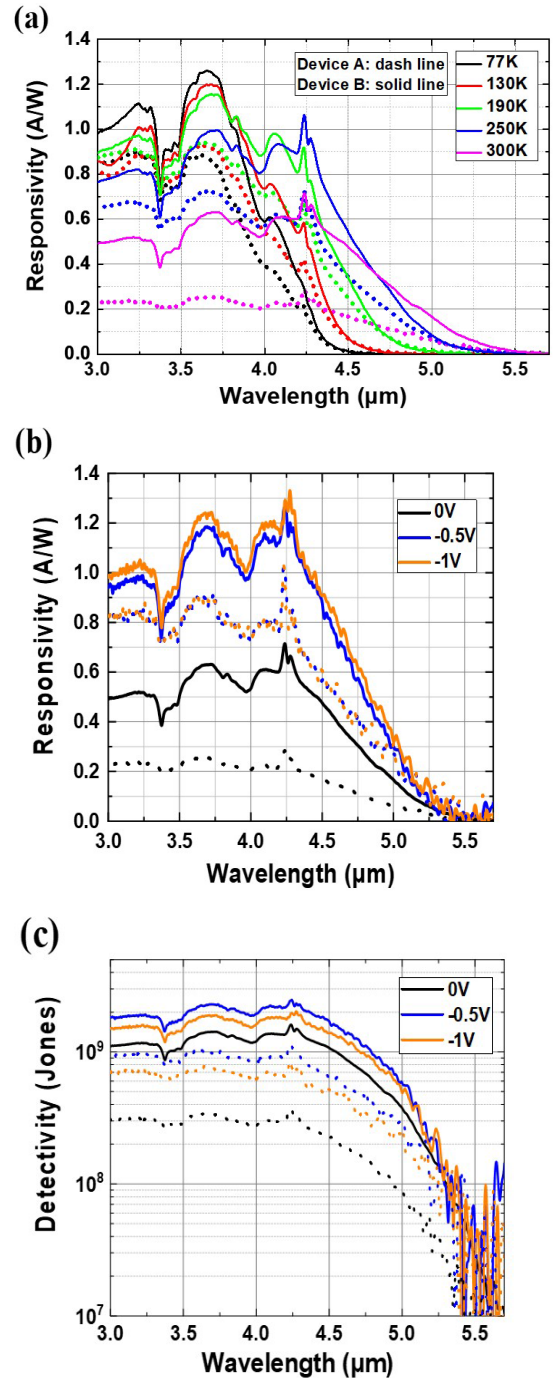


Fig. 4. (a) Responsivity under zero bias at different temperatures. Dotted line: Device A. Solid line: Device B. (b) Responsivity under different biases at 300 K. Dotted line: Device A. Solid line: Device B. (c) Johnson-noise and shot-noise-limited detectivity under different biases at 300 K. Dotted line: Device A. Solid line: Device B.

can be attributed to the higher doping in the InAs/InAsSb absorption layer, which causes a higher Auger recombination rate and a lower excess carrier lifetime [28]. Fig. 4(b) shows the responsivity of both devices under different biases at 300 K. As the bias increases, the responsivity tends to saturate and the peak responsivity of both devices is around 0.9 and 1.2 A/W at -1 V. Due to the larger dark current and smaller responsivity, Device A has a lower detectivity

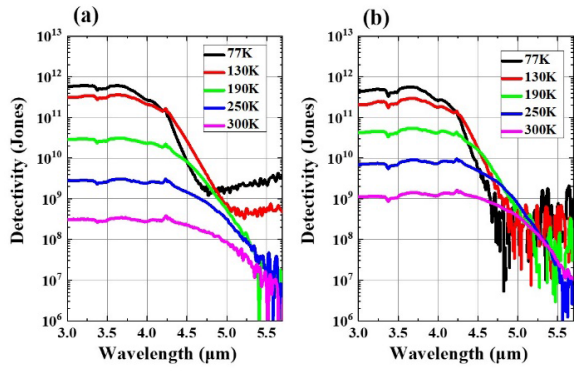


Fig. 5. Johnson-noise and shot-noise-limited detectivity under different temperatures at 0 V of (a) Device A and (b) Device B.

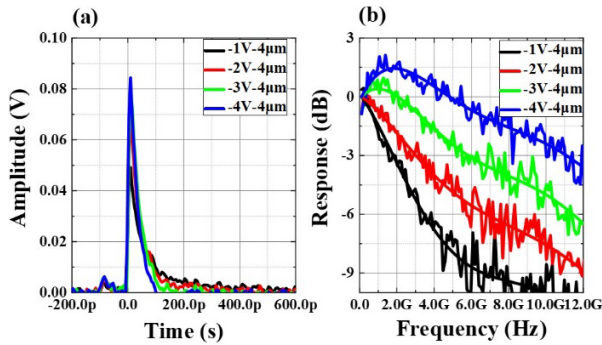


Fig. 6. (a) Pulse response of Device A under different biases at room temperature. (b) Normalized frequency response of Device A under different biases at room temperature.

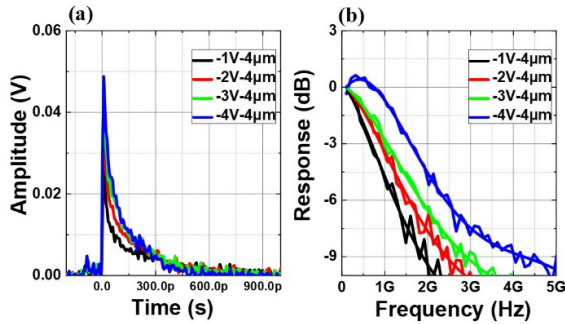


Fig. 7. (a) Pulse response of Device B under different biases at room temperature. (b) Normalized frequency response of Device B under different biases at room temperature.

than Device B. The peak detectivity is around 1×10^9 Jones for Device B at 0 V and increases to about 2×10^9 Jones at -1 V, while the peak detectivities of Device A at 0 and -1 V are about 3×10^8 and 7×10^8 Jones, respectively, as shown in Fig. 4(c). The detectivities of these two devices under different temperatures at 0 V are also shown in Fig. 5. The peak detectivity of both devices is around 6×10^{11} Jones at 77 K, which begins to decrease gradually as the temperature increases.

The high-frequency response was characterized by an optical parametric amplification (OPA) system generating wavelength-tunable MWIR pulses, as described in [24]. Figs. 6(a) and 7(a) show the pulse response of Devices A and B with a diameter of $20 \mu\text{m}$ under different biases at room

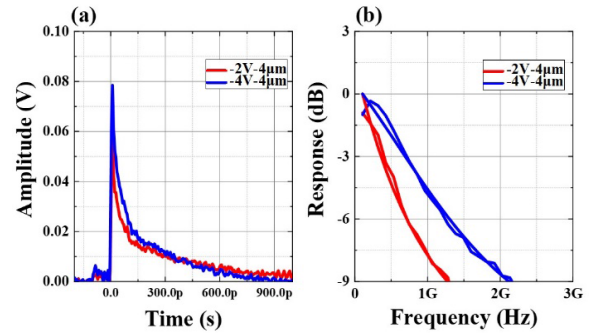


Fig. 8. (a) Pulse response of Device B under higher light intensity (compared to Fig. 7). (b) Corresponding normalized frequency response.

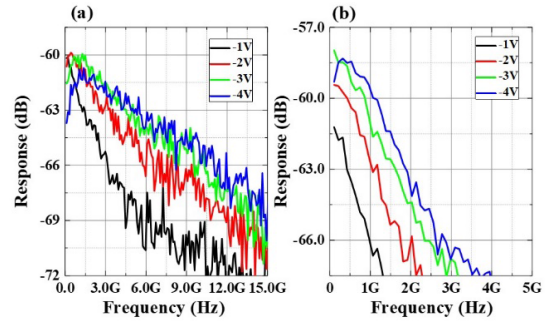


Fig. 9. Original frequency response after Fourier transforms of (a) Device A and (b) Device B.

temperature, respectively. The wavelength of OPA is around $4 \mu\text{m}$. It is observed that the electrical pulse of Device B has a much longer decay tail up to about 500 ps, whereas the decay time of Device A is about 100 ps. The slower decay in Device B compared to Device A is due to the slower hole transport in the wider depleted InAs/InAsSb absorber. The frequency response of the devices can be derived from the Fourier transform of pulse response with the loss of the RF cable, ground-signal-ground (GSG) probe, and bias-T carefully calibrated. Figs. 6(b) and 7(b) show the normalized frequency response of Devices A and B, respectively. As shown in Figs. 6 and 7, the 3-dB bandwidth of Device B is significantly lower than that of Device A. The 3-dB bandwidth of Device A is 1.81 GHz at -1 V and increases to 11.2 GHz at -4 V. For Device B, the 3-dB bandwidth is about 0.75 GHz under -1 V and rises to 1.74 GHz under -4 V. In addition, we also found that Device B could saturate more easily than Device A. As shown in Fig. 8, when the peak photocurrent of Device B is set to be close to that of Device A (in the case of Fig. 6), the fall time of the electrical pulse of Device B would be further extended. Under the bias voltage of -2 and -4 V, the 3-dB bandwidth of Device B is reduced to only 420 and 740 MHz, which is a signature of device saturation. This saturation is mainly due to the slow hole transport process in Device B, which induces a space charge effect and collapses the electrical field in the depletion region.

It is also observed that there is a peaking effect in the frequency response curve, especially at the large bias for both devices. To better understand this bandwidth behavior of both devices, Fig. 9 shows the original frequency response of the

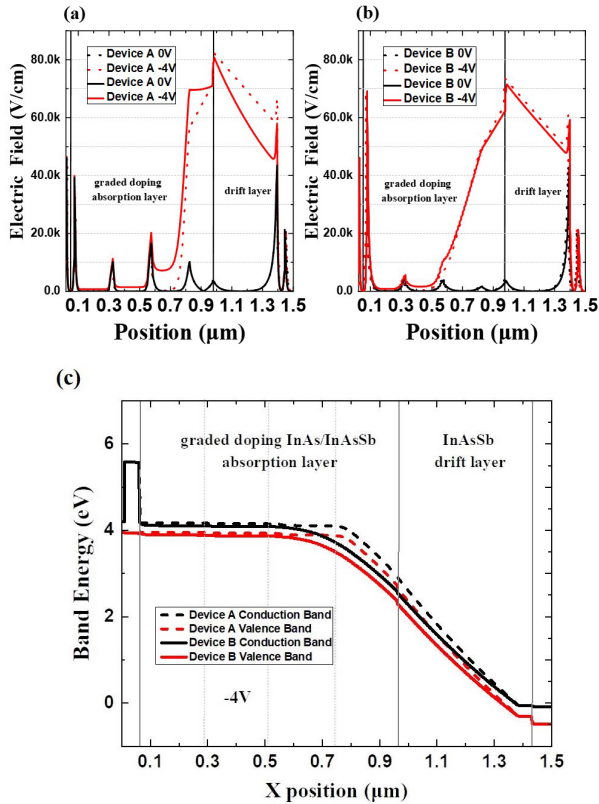


Fig. 10. Simulated electric field of (a) Device A and (b) Device B at different biases. Solid (dot) lines are the results with (without) tunneling model. (c) Band diagram of both devices under -4 -V bias. Dotted line: Device A. Solid line: Device B.

pulse response of Devices A and B after Fourier transforms without normalization. We found that for both of these devices, the response at the low-frequency range begins to decrease as the bias increases beyond -3 V, while the response at the high-frequency range keeps increasing. This bandwidth-enhancement phenomenon at high bias can be attributed to the large dark current caused by the tunneling effect. As shown in Fig. 3, the dark current of these two devices is dominated by the tunneling current at a high bias. When tunneling occurs, the excessive space charge due to tunneling enhances the recombination rate of photocarriers, resulting in a reduction of dc photocurrent and, thus, a decrease in the low-frequency part of the frequency response. In addition, the large amounts of space charge due to tunneling current will also generate a quasi-electric field [29] in the initially electrically neutral p-doped absorption region. The photogenerated carriers in the absorption region will be accelerated under this quasi-electric field, which induces an increase in response at the high-frequency range. Since Device A has a larger tunneling dark current, the bandwidth-enhancement phenomenon is more evident. To validate the explanation, the electric field of these two devices was simulated using commercial software Silvaco TCAD with or without the tunneling model, as shown in Fig. 10(a) and (b). As expected, at high bias voltages, the addition of the tunneling model could change the electric field distribution of the devices significantly. With the tunneling model included, the electric field begins to emerge

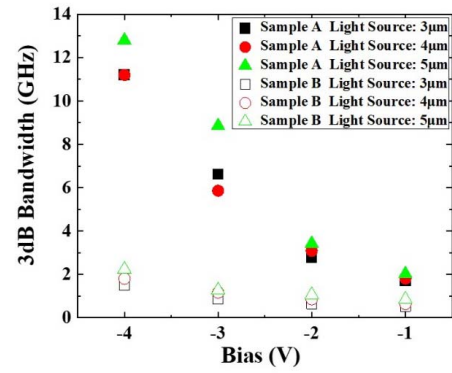


Fig. 11. 3-dB bandwidth measured at different light sources' wavelength of devices.

TABLE I
FITTING PARAMETERS

Device	Bias (V)	C_j (fF)	R_i (Ohm)	R_c (Ohm)	C_p (fF)
Device A	-1	50	4038	239	57
Device A	-4	44	806	216	57
Device B	-1	25	5123	443	44
Device B	-4	17	2798	400	44

in the initially neutral p-doped absorption region due to the accumulation of extra space carriers as reverse bias increases. Fig. 10(c) shows the simulated band diagram of Devices A and B at a high bias of -4 V. The energy band slope in the depleted absorption region of Device A is higher than that of Device B, which indicates a higher electrical field and faster tunneling in Device A, resulting in a larger bandwidth. In addition, there is no significant difference in the electric field distribution at low bias with or without including the tunneling model since the tunneling current is not substantial at low bias.

To further investigate the high-speed performance of the devices in the MWIR range, we also measured the pulse response of the devices with different light sources' wavelengths. Since Device B is more prone to saturation, here, we measured Device B with a diameter of $30 \mu\text{m}$. Fig. 11 summarizes the measured 3-dB bandwidth with varying light sources wavelength. As can be seen, both these two devices have a larger 3-dB bandwidth at $5 \mu\text{m}$ compared to the bandwidth at 3 or $4 \mu\text{m}$, and the 3-dB bandwidth of Devices at 3 and $4 \mu\text{m}$ is very close. The different 3-dB bandwidth behaviors under various incident light wavelengths are caused by the variation of the operating mode of the devices. Here, InAsSb bulk material was used as the drift layers, which can absorb the light below $4.5 \mu\text{m}$. With 3 - or 4 - μm incident light, these devices work like p-i-n PDs instead of UTC PDs, and the transit time of excess holes in the InAsSb drift layer could slightly deteriorate the 3-dB bandwidth of devices.

Moreover, the microwave reflection parameters S_{11} of the devices were measured to explore the bandwidth limiting factor. Here, we use an RC equivalent circuit model, as shown in Fig. 12(a), to fit the measured S_{11} parameters. The extracted model parameters are listed in Table I. Fig. 12(b)–(e) shows the measured and fit S_{11} parameters of these two devices by a vector network analyzer (VNA) under -1 and -4 V. As shown

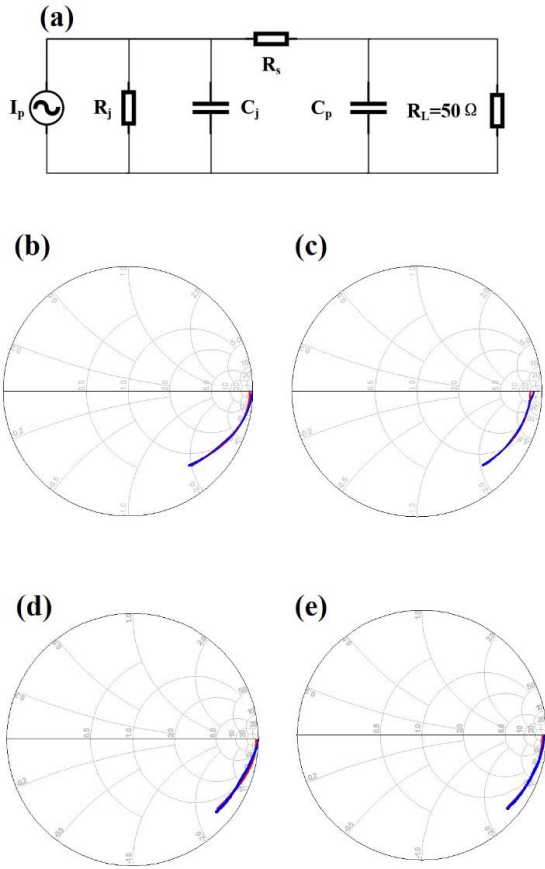


Fig. 12. (a) Equivalent circuit model used in S_{11} parameters fitting. C_j is the junction capacitance, R_j is the junction resistance, R_s is the series resistance, I_p is the ac current source, and C_p is the capacitance of the coplanar waveguide (CPW) pads. Measured (blue line) and fitting (red line) S_{11} parameters from 50 MHz to 20 GHz of Device A at (b) -1 and (c) -4 V and Device B at (d) -1 and (e) -4 V.

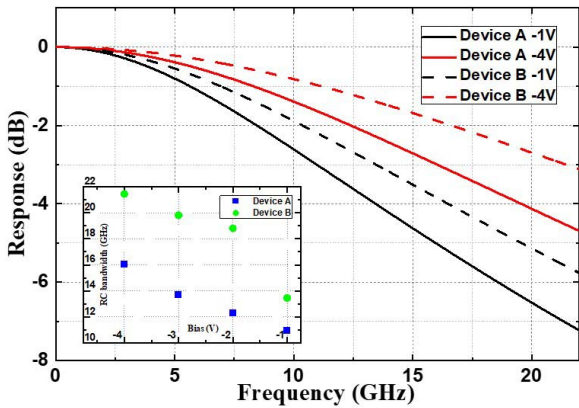


Fig. 13. Calculated RC -limited frequency response with extracted model parameters together with RC -limited bandwidths under different biases.

in Fig. 3, with reverse bias increasing to -4 V, the tunneling current quickly dominates the dark current, which decreases the PDs' shunt resistance, so the measured S_{11} curves shift to the left in the Smith chart. Fig. 13 plots the calculated RC -limited frequency response of $20\text{-}\mu\text{m}$ devices with the extracted model parameters and RC -limited 3-dB bandwidths

TABLE II
KEY MATERIAL PARAMETERS USED IN SIMULATION [30], [31]

Parameters	Value
InAs/InAsSb electron mobility	$2000\text{ cm}^2/\text{Vs}$
InAs/InAsSb hole mobility	$1(10)\text{ cm}^2/\text{Vs}$
InAs/InAsSb electron saturation velocity	$5 \times 10^6\text{ cm/s}$
InAs/InAsSb hole saturation velocity	$1 \times 10^6\text{ cm/s}$
InAsSb electron mobility	10000
InAsSb hole mobility	600
InAsSb electron saturation velocity	$8 \times 10^6\text{ cm/s}$
InAsSb hole saturation velocity	$5 \times 10^6\text{ cm/s}$
absorption coefficient at $5\mu\text{m}$	1000 cm^{-1}

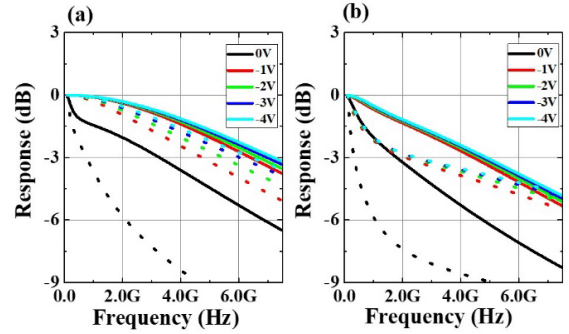


Fig. 14. Simulated carrier transit-time-limited frequency response of these two devices with different InAs/InAsSb hole mobility. (a) 10 and (b) $1\text{ cm}^2/\text{Vs}$. Solid line: Device A. Dotted line: Device B.

under different biases. The RC -limited 3-dB bandwidths are about 10.97 and 13.46 GHz at -1 V for Devices A and B, respectively. When the bias increases to -4 V, the RC -limited 3-dB bandwidth reaches 16.03 and 21.44 GHz for Devices A and B, respectively. The calculated RC -limited 3-dB bandwidth indicates that the bandwidth of Device B is limited by the carrier transit time, while the bandwidth of Device A is limited by the carrier transit time at low bias and by RC time at high bias.

According to the measured frequency response and S_{11} parameter analysis above, we can see that the carrier transit-time-limited bandwidth of Device A is significantly higher than that of Device B. To explore the limiting factor of carrier transport in the devices, we qualitatively simulate the carrier transit-time-limited frequency response of these two devices. Here, we do not consider the effect of tunneling current in the simulation, and the light source was set to $5\text{ }\mu\text{m}$. Table II shows the critical material parameters used in the simulation. Fig. 14 shows the simulated carrier transit-time-limited frequency response of these two devices with different InAs/InAsSb hole mobilities with Silvaco TCAD. Since the tunneling effect is not considered, the bandwidth of these devices does not exhibit a significant enhancement as in the experimental measurement. We found that as the hole mobility of InAs/InAsSb is set to a very small value such as $1\text{ cm}^2/\text{Vs}$, the simulated frequency response of Device B shows a significantly lower value than that of Device A. In contrast, if the hole mobility of InAs/InAsSb is set to be a larger value such as $10\text{ cm}^2/\text{Vs}$, there would be no significant difference in the carrier transit-time-limited bandwidth for these two devices. This indicates that the hole mobility of the

InAs/InAsSb material system should be fairly small, which is consistent with the value from the reported literature [30], [31]. Moreover, it also suggests that the transit time of the device could often be limited by the slow hole drift velocity.

Based on the analysis above, to achieve a large bandwidth of InAs/InAsSb UTC PDs, we should avoid the holes drifting at a lower velocity in the InAs/InAsSb SLs. In other words, it is more inclined to have undepleted InAs/InAsSb SLs to enjoy the fast dielectric relaxation of holes. However, the doping concentration of InAs/InAsSb SLs should be carefully optimized not to deteriorate the carrier lifetime significantly.

IV. CONCLUSION

In conclusion, we have studied the high-speed InAs/InAsSb T2SL MWIR PDs based on UTC structure in this work. Two device structures with different absorber doping levels are comprehensively investigated and compared. The cutoff wavelength of these two devices is around $5.5 \mu\text{m}$ at room temperature. Benefiting from more uniform electric field distribution and lower carrier recombination rates, the device with a lower doped absorber has a lower dark current and higher responsivity performance. However, the low hole mobility of InAs/InAsSb SL will result in a longer hole carrier transit time in the lower doped absorber and thus reduces the 3-dB bandwidth of Device B. From the perspective of improving the bandwidth and detectivity simultaneously, the InAs/InAsSb UTC PDs need to be optimized to accelerate the hole carrier transit time and maintain a long carrier lifetime.

ACKNOWLEDGMENT

The authors would like to thank the device fabrication support from the ShanghaiTech University Quantum Device Lab.

REFERENCES

- [1] O. Spitz et al., "Free-space communication with directly modulated mid-infrared quantum cascade devices," *IEEE J. Sel. Topics Quantum Electron.*, vol. 28, no. 1, pp. 1–9, Jul. 2022, doi: [10.1109/JSTQE.2021.3096316](https://doi.org/10.1109/JSTQE.2021.3096316).
- [2] A. Delga and L. Leviandier, "Free-space optical communications with quantum cascade lasers," *Proc. SPIE*, vol. 10926, Feb. 2019, Art. no. 1092617.
- [3] X. Pang et al., "Free-space communications enabled by quantum cascade lasers," *Phys. Status Solidi A*, vol. 218, no. 3, Feb. 2020, Art. no. 2000407, doi: [10.1002/pssa.202000407](https://doi.org/10.1002/pssa.202000407).
- [4] C. Bao et al., "Architecture for microcomb-based GHz-mid-infrared dual-comb spectroscopy," *Nature Commun.*, vol. 12, no. 1, p. 6573, Nov. 12 2021, doi: [10.1038/s41467-021-26958-6](https://doi.org/10.1038/s41467-021-26958-6).
- [5] L. A. Sterczewski et al., "Mid-infrared dual-comb spectroscopy with interband cascade lasers," *Opt Lett*, vol. 44, no. 8, pp. 2113–2116, Apr. 15 2019, doi: [10.1364/OL.44.002113](https://doi.org/10.1364/OL.44.002113).
- [6] G. Villares, A. Hugi, S. Blaser, and J. Faist, "Dual-comb spectroscopy based on quantum-cascade-laser frequency combs," *Nature Commun.*, vol. 5, no. 1, pp. 1–9, Dec. 2014.
- [7] B. Meng et al., "Mid-infrared frequency comb from a ring quantum cascade laser," *Optica*, vol. 7, no. 2, pp. 162–167, 2020, doi: [10.1364/optica.377755](https://doi.org/10.1364/optica.377755).
- [8] E. Rodriguez et al., "Room-temperature, wide-band, quantum well infrared photodetector for microwave optical links at $4.9 \mu\text{m}$ wavelength," *ACS Photon.*, vol. 5, no. 9, pp. 3689–3694, 2018, doi: [10.1021/acsp Photonics.8b00704](https://doi.org/10.1021/acsp Photonics.8b00704).
- [9] J. Hillbrand et al., "High-speed quantum cascade detector characterized with a mid-infrared femtosecond oscillator," *Opt. Exp.*, vol. 29, no. 4, pp. 5774–5781, 2021, doi: [10.1364/oe.417976](https://doi.org/10.1364/oe.417976).
- [10] J. Huang, Z. Xie, Y. Chen, J. E. Bowers, and B. Chen, "High speed mid-wave infrared uni-traveling carrier photodetector," *IEEE J. Quantum Electron.*, vol. 56, no. 4, pp. 1–7, Aug. 2020.
- [11] Y. Chen, Z. Xie, J. Huang, Z. Deng, and B. Chen, "High-speed uni-traveling carrier photodiode for $2 \mu\text{m}$ wavelength application," *Optica*, vol. 6, no. 7, pp. 884–889, 2019.
- [12] T. Ishibashi and H. Ito, "Uni-traveling-carrier photodiodes," *J. Appl. Phys.*, vol. 127, no. 3, Jan. 2020, Art. no. 031101.
- [13] Z. Li, H. Pan, H. Chen, A. Beling, and J. C. Campbell, "High-saturation-current modified uni-traveling-carrier photodiode with cliff layer," *IEEE J. Quantum Electron.*, vol. 46, no. 5, pp. 626–632, May 2010.
- [14] Z. Li et al., "High-power high-linearity flip-chip bonded modified uni-traveling carrier photodiode," *Opt. Exp.*, vol. 19, no. 26, pp. B385–B390, 2011.
- [15] Z. Xie, Z. Zhou, L. Li, Z. Deng, H. Ji, and B. Chen, "High-speed 850 nm photodetector for zero-bias operation," *IEEE J. Sel. Topics Quantum Electron.*, vol. 28, no. 2, pp. 1–7, Jul. 2021.
- [16] Z. Li, H. Pan, H. Chen, A. Beling, and J. C. Campbell, "High-saturation-current modified uni-traveling-carrier photodiode with cliff layer," *IEEE J. Quantum Electron.*, vol. 46, no. 5, pp. 626–632, Jun. 2010.
- [17] Q. Li et al., "High-power flip-chip bonded photodiode with 110 GHz bandwidth," *J. Lightw. Technol.*, vol. 34, no. 9, pp. 2139–2144, May 1, 2016.
- [18] E. Steenbergen et al., "Significantly improved minority carrier lifetime observed in a long-wavelength infrared III-V type-II superlattice comprised of InAs/InAsSb," *Appl. Phys. Lett.*, vol. 99, no. 25, Dec. 2011, Art. no. 251110.
- [19] L. She et al., "Mid-wave infrared $\text{p}^+\text{-Bn}$ InAs/InAsSb type-II superlattice photodetector with an AlAsSb/InAsSb superlattice barrier," *Infr. Phys. Technol.*, vol. 121, Mar. 2022, Art. no. 104015.
- [20] G. Deng et al., "High operating temperature pBn barrier mid-wavelength infrared photodetectors and focal plane array based on InAs/InAsSb strained layer superlattices," *Opt. Exp.*, vol. 28, no. 12, pp. 17611–17619, 2020.
- [21] D. Z. Ting et al., "Long and very long wavelength InAs/InAsSb superlattice complementary barrier infrared detectors," *J. Electron. Mater.*, vol. 51, pp. 1–9, Mar. 2022.
- [22] D. Wu, J. Li, A. Dehzangi, and M. Razeghi, "High performance InAs/InAsSb type-II superlattice mid-wavelength infrared photodetectors with double barrier," *Infr. Phys. Technol.*, vol. 109, Sep. 2020, Art. no. 103439.
- [23] H. Kim et al., "Long-wave infrared nBn photodetectors based on InAs/InAsSb type-II superlattices," *Appl. Phys. Lett.*, vol. 101, no. 16, Oct. 2012, Art. no. 161114.
- [24] J. Huang et al., "High-speed mid-wave infrared uni-traveling carrier photodetector based on InAs/InAsSb type-II superlattice," *IEEE Electron Device Lett.*, vol. 43, no. 5, pp. 745–748, Mar. 2022.
- [25] Z. Xie, Z. Deng, X. Zou, and B. Chen, "InP-based near Infrared/Extended-short wave infrared dual-band photodetector," *IEEE Photon. Technol. Lett.*, vol. 32, no. 16, pp. 1003–1006, Aug. 15, 2020.
- [26] Y. Teng et al., "Demonstration of MOCVD-grown long-wavelength infrared InAs/GaSb superlattice focal plane array," *IEEE Access*, vol. 9, pp. 60689–60694, 2021, doi: [10.1109/access.2021.3072845](https://doi.org/10.1109/access.2021.3072845).
- [27] Z. Xie et al., "High-speed mid-wave infrared interband cascade photodetector at room temperature," *Opt. Exp.*, vol. 28, no. 24, pp. 36915–36923, 2020.
- [28] Y. Aytac et al., "Bandgap and temperature dependence of Auger recombination in InAs/InAsSb type-II superlattices," *J. Appl. Phys.*, vol. 119, no. 21, Jun. 2016, Art. no. 215705, doi: [10.1063/1.4953386](https://doi.org/10.1063/1.4953386).
- [29] T. Ishibashi, S. Kodama, N. Shimizu, and T. Furuta, "High-speed response of uni-traveling-carrier photodiodes," *Jpn. J. Appl. Phys.*, vol. 36, no. 10, pp. 6263–6268, Oct. 1997, doi: [10.1143/jjap.36.6263](https://doi.org/10.1143/jjap.36.6263).
- [30] A. Soibel, D. Z. Ting, A. M. Fisher, A. Khoshkhalgh, B. Pepper, and S. D. Gunapala, "Temperature dependence of diffusion length and mobility in mid-wavelength InAs/InAsSb superlattice infrared detectors," *Appl. Phys. Lett.*, vol. 117, no. 23, Dec. 2020, Art. no. 231103.
- [31] L. K. Casias et al., "Vertical carrier transport in strain-balanced InAs/InAsSb type-II superlattice material," *Appl. Phys. Lett.*, vol. 116, no. 18, p. 182109, 2020.